Gravity and inertia in quantum mechanics

J.-L. Staudenmann and S. A. Werner

Physics Department and Research Reactor Facility, University of Missouri-Columbia, Columbia, Missouri 65211

R. Colella and A. W. Overhauser

Physics Department, Purdue University, West Lafayette, Indiana 47907

The experiments described in this paper probe the simultaneous effects of gravity, inertia, and quantum mechanics on the motion of the neutron. Using a neutron interferometer of the type developed by Bonse and Hart for x rays, we have observed quantum-mechanical interference phenomena induced by the gravitational field of the Earth and by the Earth's rotation relative to the fixed stars. The importance of these experiments with regard to the role of the principle of equivalence in quantum mechanics is discussed.

I. INTRODUCTION

The purpose of this paper is to provide a comprehensive description of a series of neutron-interferometry experiments we have carried out over the last few years, in which the effects of gravity and inertia on the quantum-mechanical phase of the neutron have been studied. Separate preliminary reports on various aspects of this work have already been published.[1-5] We will review in this paper all of our previous work and give many experimental and theoretical details that have not been discussed in our previous reports.

In 1965 it was demonstrated by Bonse and Hart[6] that interference effects could be obtained between well-separated coherent beams of x-ray photons of about 1-Å wavelength. In their experiment an x-ray beam was split into two spatially separated coherent beams, a few centimeters apart, and recombined in such a way that intensity oscillations could be observed as the optical path along one of the beams was changed. This remarkable achievement opened up the field of interferometry in the angstrom region. The question was immediately asked whether or not the same principles could be used to get interference effects between coherent beams of thermal neutrons, which can be diffracted in crystals in the same way as x rays. The feasibility of neutron interferometry was, in fact, finally demonstrated in 1974 by Rauch, Treimer, and Bonse,[7] using essentially the same scheme, apart from dimensions, adopted for x rays. The principles upon which x-ray and neutron interferometry are based are obviously very different from those applied in optical interferometry. Two new features are at the basis of interferometry in the angstrom region: (a) Bragg diffraction, and (b) highly perfect crystals, free of lattice defects. The usual requirements in

polishing and aligning optical surfaces to fractions of wavelength would obviously not be satisfiable in x-ray and neutron interferometry. We will see, however, in the next section how the very same two new features (a) and (b) above enable us to circumvent this apparently insurmountable difficulty. When a neutron beam is coherently split and recombined, a new property of the neutron becomes available for investigation: the phase. In the language of quantum mechanics we can say that it is the wave function, along with its own phase, that becomes measurable, whereas before the advent of neutron interferometry only the probability density $|\psi|^2$ could be measured. A number of experiments have been performed since 1974 in which the neutron phase has been probed in one way or another.[8] We will concentrate in this paper on those experiments in which the neutron phase is affected by the Earth's gravity and by its rotation. Among the various interactions in nature, gravity is by far the weakest one. In the hydrogen atom, for example, the gravitational attraction between the proton and the electron is only 10^{-40} times the electrostatic (Coulomb) attraction. The fact that neutrons are subject to a gravitational pull toward the center of the Earth has been demonstrated by verifying that a neutron beam follows a parabolic trajectory.[9]

The gravitational constant involved in interpreting the observed parabolic paths has been verified to coincide, with reasonable accuracy, with the accepted value for the gravitational accelerations as measured with macroscopic bodies. This result has been obtained in a recent improved version of this experiment.[10] The important result here is that the gravitational mass of the neutron is found to coincide with its intertial mass, as required by the principle of equivalence. This principle has been verified with great accuracy,

better than 1 part in 10^{13}, for macroscopic bodies.[11] There is no guarantee, however, that the same principle holds for the quantum-mechanical behavior of isolated elementary particles. We want to emphasize that the parabolic fall of a neutron is a *classical experiment*, in the sense that no quantum features of the neutron are being observed. This would merely be a requirement imposed by the correspondence principle.

The experiment which we have carried out is one in which a neutron interferometer is oriented in such a way that the two coherent beams, into which the primary beam is split, propagate in regions of space with different average gravitational potential. A gravity-induced change of phase provides a manifestation of gravity effects on a quantum-mechanical feature of the neutron. If the change of phase agrees with a gravitational potential of the form $m_g \vec{g} \cdot \vec{r}$, where m_g is the gravitational mass of the neutron, $\vec{g}$ is the gravitational acceleration, and $\vec{r}$ is the position vector of the neutron, then we can conclude that we have verified the principle of equivalence for neutrons *in the quantum limit*. It will be shown, in fact, that the fringe shift can be expressed by a formula in which the gravitational constant and Planck's constant are inseparably linked. This is, to our knowledge, the only experiment in physics in which the outcome depends on a simultaneous direct combination of gravitational and quantum-mechanical properties of an elementary particle.

A complete test of the principle of equivalence in the quantum limit would involve repeating the experiment in an accelerated frame of reference, traveling in a gravitation-free space. We have not directly done this experiment. However, we surmise that this experiment does not need to be done, if we believe that the Schrödinger equation holds in an accelerated frame. In such a case, it is possible to derive the same expression for the fringe shift as that obtained for the gravitational case.[12]

Since the coordinate frame in which our experiments are carried out is not an intertial frame, the Hamiltonian governing the neutron's motion will involve a third term in addition to the kinetic energy (relative to the Earth) and the gravitational potential energy. Our neutron experiment designed to detect this effect is the quantum-mechanical analog of the optical interferometry experiment of Michelson, Gale, and Pearson[13] carried out in 1925. An experiment which demonstrated the principles of detection of rotation by optical interferometry was carried out earlier in 1913 by Sagnac.[14] The physical principle involved forms the basis for the ring-laser Sagnac gyroscope.

In the latest version of our experiments, a geo-metry has been chosen in which the effect of gravity is suppressed. In this way only effects associated with the relative motion of the Earth with respect to the stars is detected. If our results agree with the insertion in the neutron Hamiltonian of a term of the form $\vec{\omega} \cdot \vec{L}$ (where $\vec{\omega}$ is the Earth's angular rotational velocity, and $\vec{L}$ is the neutron's angular momentum with respect to the center of the Earth) we can conclude that the principle of equivalence for neutrons has been verified in the quantum limit, in an accelerated frame free of gravity.

In the next section we will discuss the basic principles of neutron interferometry. In Sec. III we will give some experimental details relevant to the neutron source, the neutron monochromator, the detection system, and the construction of the interferometer. In Sec. IV we give the theoretical background necessary to understand the experimental results. Section V is devoted primarily to a discussion of gravitationally-induced quantum interference. The experiments discussed in this section were carried out with an incident beam directed horizontally, that is, parallel to the local surface of the Earth. The effect of the rotation of the Earth on the neutron phase has been accurately detected with a vertically directed incident beam. These experiments are discussed in Sec. VI. In Sec. VII we make some concluding remarks.

II. PRINCIPLES OF NEUTRON INTERFEROMETRY

Various schemes have been proposed, and in part realized, for obtaining interference effects between spatially separated coherent neutron beams having a wavelength in the angstrom range.[15] We will limit ourselves to consider the scheme depicted in Fig. 1, consisting of three identical perfect silicon crystal slabs cut perpendicular to a set of strongly reflecting lattice planes, typically (220). The distances d_1 and d_2 between the slabs are usually a few centimeters and are equal to within about 1 μm. A nominally collimated, monochromatic beam is directed along the line SA and is coherently split by the first silicon crystal slab by Bragg reflection. These two coherent beams are again split in the second crystal in the regions near points B and C. Two of these beams overlap and interfere near point D in the third Si Slab. We always assume that by "beam" we mean a plane wave of limited, but not infinitesimal, lateral extent (a few mm or so). If the beam traversing the path I is phase shifted by increasing the "optical" path length (via some interaction potential) relative to the beam traversing the path II, the intensities in the detectors C_2 and C_3 will
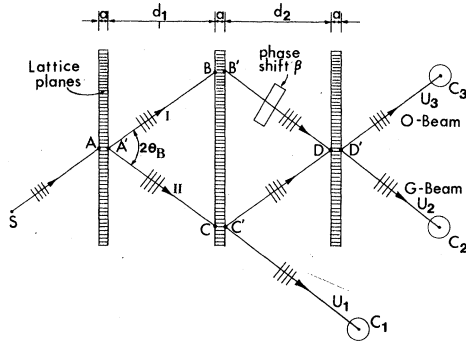
FIG. 1. A schematic diagram of the LLL interfero-
meter. The incident beam is coherently split in the re-
gion of the first slab between A and A′. The two coher-
ent beams I and II are again coherently split in the sec-
ond crystal slab and recombined in the third crystal in
the region of points D and D′. The interfering beams
are detected by counters C_2 and C_3; a noninterfering
beam is detected by counter C_1.

change. We will show here that the expected in-
tensities in these detectors, as a function of the
phase shift β are of the form

$$I_2 = \gamma - \alpha \cos\beta \tag{1}$$

and

$$I_3 = \alpha(1 + \cos\beta), \tag{2}$$

The constants α and γ depend upon the incident
flux, the crystal structure and the neutron-nuclear
scattering length of Si.

The basic principle of this interferometer seems
simple enough; however, there are certain sub-
tleties hidden in the apparent simplicity. The
first one concerns the alignment of the three crys-
tals. Clearly, in order to preserve the Bragg
reflecting condition for a given wavelength neu-
tron, we must align the three crystals to within
the "Darwin width," which is typically 0.1″ of arc
for neutrons. Bonse and Hart[6] devised a simple
and ingenious way to achieve this result. They
cut out the three slabs from a large monolithic
silicon single crystal of very high quality, free of
lattice defects of any kind. As a consequence of
great advances in crystal growth techniques,
prompted by the needs of the solid-state-elec-
tronics industry, it is possible today to purchase
from commercial manufacturers silicon crystals
of the required perfection with typical dimensions
of order 5 to 10 cm. Spatial coherence in atomic
positions is preserved to a billionth of a centi-
meter over these distances.

The second point concerns the accuracy with
which the surfaces of the slabs need to be polish-
ed. It would clearly be impossible to satisfy the
usual requirements of optical interferometry, in

which the surfaces of the optical components need
to be polished to fractions of wavelength. The
phase shift resulting from a step of thickness t on
the surface is given by the formula

$$\beta_{step} = (2\pi/\lambda)(n-1)t, \tag{3}$$

where λ is the neutron wavelength and n is the
index of refraction, which differs from 1 by

$$n - 1 = \frac{\lambda^2}{2\pi}Nb. \tag{4}$$

Here N is the atom density and b is the neutron-
nuclear scattering length. For Si at $\lambda = 1.4$ Å,
$(n-1) = 0.67 \times 10^{-6}$. Thus, a step $t = 2\,\mu$m will
cause a phase shift corresponding to $\frac{1}{100}$th of a
fringe.

The third consideration is the question of the
extent to which the incident beam is required to be
monochromatic. In our neutron-interferometry
experiments, the incident beam is only nominally
monochromatic with $\Delta\lambda/\lambda \approx 0.01$. The important
feature of this type of interferometer is that it
utilizes Bragg reflection from perfect crystals.
This requires the wavelength, along a given tra-
jectory (ray line) to be defined to within about 1
part in 10^6. But this definition of wavelength is
accomplished by the interferometer itself and not
through the preparation of the incident beam.

The final point we want to mention is a peculiar
feature of angstrom-wavelength interferometry.
We can understand that the two beams BD and CD
in Fig. 1 are coherent and produce interference
fringes localized in space, with spatial separa-
tions of order 1 Å. Strictly speaking, the inter-
ferometer could consist of the first two slabs
only. The problem is that no film or detector of
any kind is able to resolve fringes so closely sep-
arated in the region of the overlap. The scheme
adopted by Bonse and Hart is to use the third
crystal as a receiver, or as a mixer. The crys-
tal lattice potential $V_{\vec{G}}$ corresponding to the re-
ciprocal lattice vector $\vec{G}$ mixes the two waves
traveling along the rays BD and CD, so that the
outgoing beams depend upon the wave amplitudes
of each of the incident beams.

We will now look in detail at the diffraction
mechanism of the three crystal LLL interfero-
meter. (LLL stands for Laue-Laue-Laue trans-
mission geometry.) The theory of diffraction of
neutron waves by the periodic potential of a per-
fect crystal lattice is similar in many ways to the
theory of electron motion in solids. A neutron
wave of wave vector $\vec{K}_0^{\nu}$ oriented on or near a
Brillouin-zone boundary will be Bragg reflected
forming a coherent state described by the wave
function

$$\psi_\gamma(\vec{r}) = \psi_0^\gamma \exp(i\vec{K}_0^\gamma \cdot \vec{r}) + \psi_G^\gamma \exp[i(\vec{K}_0^\gamma + \vec{G}) \cdot \vec{r}]. \quad (5)$$

In electron band theory, there will be two such wave functions, one for states above the energy gap corresponding to the reciprocal lattice vector $\vec{G}$, and one below the energy gap. In the dynamical theory of neutron diffraction, the energy of the neutron is fixed by the preparation of the incident beam, and the periodic potential causes a splitting of the allowed internal wave vectors $\vec{K}_0^\gamma$. Thus, the index γ takes on two possible values. The wave amplitudes ψ_G^γ are determined by the orientation of the external incident wave vector $\vec{k}_0$ and the requirements of continuity of the neutron wave function across the entrant boundary. Continuity of the wave function across the exit boundary determines the amplitudes of the diffracted beam (χ_G) and the forward scattered beam (χ_0), such that the wave function of the neutron leaving the crystal is of the form

$$\chi(\vec{r}) = \chi_0 \exp(i\vec{k}_0 \cdot \vec{r}) + \chi_G \exp(i\vec{k}_G \cdot \vec{r}). \quad (6)$$

For the symmetric Laue geometry, the solution to this problem is given in the Appendix. The results are given by Eqs. (A21) and (A22); they are of the form

$$\chi_0 = T(\Delta\theta)\Phi \quad (7)$$

and

$$\chi_G = D(\Delta\theta)\Phi, \quad (8)$$

where Φ is the amplitude of the incident plane wave, and the coefficients T and D depend upon the angular deviation $\Delta\theta$ of the incident wave vector $\vec{k}_0$ from the exact Bragg condition for the reciprocal lattice point $\vec{G}$.

Using these results, it is an easy matter to derive expressions for the waves emerging from the third slab of the interferometer. The wave function in the region of detector C_3 is

$$U_3(\vec{r}) = \Phi\{D(\Delta\theta) \exp(i\vec{k}_0 \cdot \vec{r}_C)D(-\Delta\theta) \exp[i\vec{k}_0 \cdot (\vec{r}_D - \vec{r}_C)]T(\Delta\theta)$$
$$+ T(\Delta\theta) \exp(i\vec{k}_0 \cdot \vec{r}_B)D(\Delta\theta) \exp[i\vec{k}_G \cdot (\vec{r}_D - \vec{r}_B)]D(-\Delta\theta)e^{i\beta}\} \exp[i\vec{k}_0 \cdot (\vec{r} - \vec{r}_D)], \quad (9)$$

and the wave function in the region of detector C_2 is

$$U_2(\vec{r}) = \Phi\{D(\Delta\theta) \exp(i\vec{k}_G \cdot \vec{r}_C)D(-\Delta\theta) \exp[i\vec{k}_0 \cdot (\vec{r}_D - \vec{r}_C)]D(\Delta\theta)$$
$$+ T(\Delta\theta) \exp(i\vec{k}_0 \cdot \vec{r}_B)D(\Delta\theta) \exp[i\vec{k}_G \cdot (\vec{r}_D - \vec{r}_B)]T(-\Delta\theta)^{i\beta}\} \exp[i\vec{k}_G \cdot (\vec{r} - \vec{r}_D)]. \quad (10)$$

The origin of coordinates is taken to be point A in Fig. 1. The phase shift β is assumed to be introduced into path I of the interferometer. The external diffracted wave vector $\vec{k}_G$ is given by Eq. (A29). After some algebra, we find for squares of the wave amplitudes

$$|U_3|^2 = |\Phi|^2(1 + \cos\beta)2A(x, \epsilon) \quad (11)$$

and

$$|U_2|^2 = |\Phi|^2[B(x, \epsilon) - 2A(x, \epsilon)\cos\beta]. \quad (12)$$

The functions A and B are given by

$$A(x, \epsilon) = \frac{1}{(x^2 + 1)^3} \sin^4 \xi(x^2 + \cos^2 \xi) \quad (13)$$

and

$$B(x, \epsilon) = \frac{1}{(x^2 + 1)^3} \sin^2 \xi[(x^2 + \cos^2 \xi)^2 + \sin^4 \xi]. \quad (14)$$

The definition of the symbol ξ is given by Eq. (A23). These functions are dependent upon the two dimensionless parameters

$$x = \eta/p = \frac{k_0^2 \sin2\theta_B V_{cell}}{4\pi |F_G|} \Delta\theta \quad (15)$$

and

$$\epsilon = \frac{pa}{2\cos\theta_B} = \frac{2\pi |F_G| a}{V_{cell} k_0 \cos\theta_B}. \quad (16)$$

Here θ_B is the Bragg angle, V_{cell} is the volume of a unit cell, F_G is the structure factor, and a is the slab thickness.

Since the beam incident on the interferometer is divergent, we must integrate these expressions over the angle $\Delta\theta$. This is equivalent to integrating over the scaled angular variable x. We, therefore, see that the expressions for the parameters α and γ in Eqs. (1) and (2) are

$$\alpha = I_0 \frac{8\pi |F_G|}{k_0^2 \sin2\theta_B V_{cell}} \int_{-\infty}^{\infty} A(x, \epsilon)dx \quad (17)$$

and

$$\gamma = I_0 \frac{4\pi |F_G|}{k_0^2 \sin2\theta_B V_{cell}} \int_{-\infty}^{\infty} B(x, \epsilon)dx, \quad (18)$$

where I_0 is the incident beam intensity. The integrals appearing in Eqs. (17) and (18) are shown in Fig. 2. For our experiments $a = 0.246$ cm, at $\lambda = 1.4$ Å, the value of $\epsilon \approx 40$, which gives $\gamma/\alpha \approx 2.6$. Thus the predicted contrast in the "O-beam" is considerably higher than in the "G-beam", as observed experimentally.

The analysis presented here assumes that each plane wave Fourier component in the incident di-
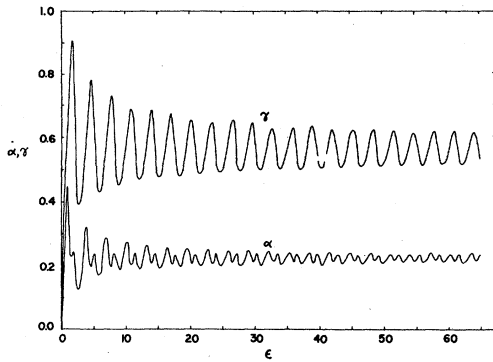
FIG. 2. Dependence of the coefficients α and γ in the counting rate Eqs. (1) and (2) on ϵ. ϵ is given by Eq. (16) and α and γ are ploted in units of $I_0 4\pi |F_G| / k_0^2 \sin 2\theta_B V_{cell}$. See Eqs. (17) and (18).

vergent beam is not phase correlated with other Fourier components. That is, we are assuming an incoherent superposition of plane waves. This may not in general be the case. Alternatively, one might assume that the incident beam is a monochromatic spherical wave, for which the Fourier decomposition into plane waves is well known. The theory of the interferometer based on spherical waves has been worked out in detail by Bauspiess, Bonse, and Graeff.[16] However, according to Parseval's theorem the integrated intensities are independent of the phase correlations in the incident beam. Only the intensity distribution across the beams will reflect these details. Since our detectors integrate over the en-

tire width of the outgoing beams, we need not concern ourselves with these details.

In order to appreaciate the requirements on precision in machining an interferometer, analysis of the type given here should be carried out for a defocused interferometer; that is, one in which the distances d_1 and d_2 in Fig. 1 are not equal. Analysis of this type has been carried out in Ref. 16, and some beautiful x-ray experiments demonstrating defocusing were carried out earlier by Bonse and teKaat.[17] The conclusion is that a neutron interferometer must be machined to an accuracy of about 1 μm to achieve nearly perfect contrast.

III. DESCRIPTION OF THE EXPERIMENTAL APPARATUS

The experiments which are described here have been carried out at the 10-MW University of Missouri Research Reactor. Figure 3 shows a general layout of the experimental apparatus. A monochromatic beam is produced in a double crystal monochromator assembly which utilizes two pyrolytic graphite crystals. This monochromator produces a variable energy monochromatic beam which is collimated to 0.7° and allowed to pass through a fission chamber beam monitor and several slits onto the neutron interferometer. The double crystal arrangement allows us to keep the direction of the monochromatic beam fixed relative to the Earth, at all wavelengths. At a wavelength $\lambda = 1.4$ Å the monochromatic beam intensity
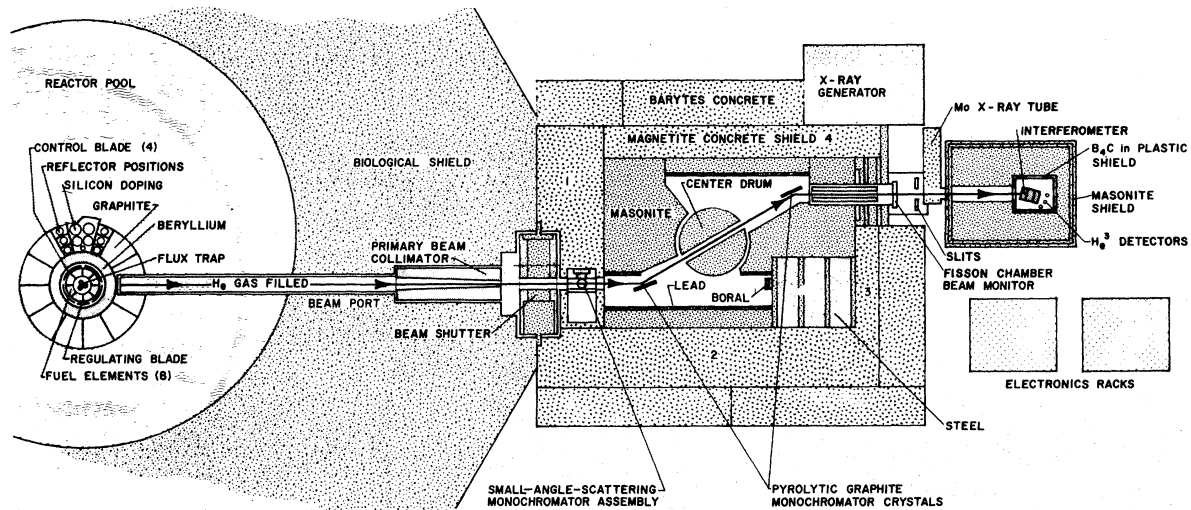
DOUBLE-CRYSTAL SPECTROMETER AND NEUTRON INTERFEROMETER AT BEAM PORT B - MURR

FIG. 3. Schematic diagram of the entire apparatus, including the reactor core, the primary and secondary collimators, the double-crystal monochromator, and the interferometer.
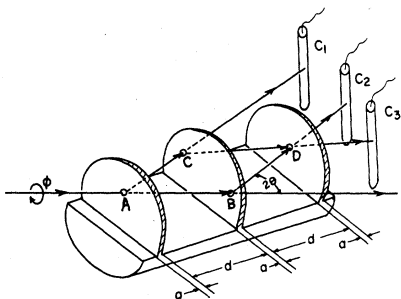
FIG. 4. Schematic diagram of the neutron interfero-meter and the ^{3}He detectors used in these experiments.

is about 2×10^6 neutrons/cm^2/sec. Three small ^{3}He detectors are mounted behind the interfero-meter, inside an aluminum box ($25 \times 25 \times 25$ cm^3) which is attached to a rotator assembly. The ^{3}He detectors have a diameter of $\frac{1}{4}$ in. and are filled to a pressure of 40 atm, yielding a counting effi-ciency of order 90% for thermal neutrons. Fig-ure 4 shows the arrangements of the three count-ers, with C_1 mounted on a noninterfering beam for the purpose of aiding in orienting the inter-ferometer. Occasionally the three ^{3}He counters are replaced by a single Ar-filled proportional counter when x rays are used instead of neutrons. The rotator assembly, consisting of a large steel tube supported on ball bearings, is rigidly attach-ed to the inside of a large dense masonite neutron shield which is mounted on a vibration isolation pad.

A. The neutron wavelength λ_0

The interpretation of all our experiments re-quires an accurate knowledge of the incident neu-tron wavelength λ_0 as measured in the laboratory frame of reference. We have employed a techni-que to measure λ_0 which is schematically illus-trated in Fig. 5. A pyrolytic graphite crystal is placed in the beam which passes directly through the interferometer. The beam transmitted through this crystal is counted with a fission chamber. By rotating the pyrolytic graphite crystal through the same (004) reflection used for monochroma-tion of the incident neutrons, a dip in the trans-mission is observed. A similar dip is observed by reflecting the beam to the right instead of to the left. The difference in the crystal rotation angles for minimum transmission, i.e., $\theta_2 - \theta_1$, determines the neutron wavelength in terms of the lattice parameter of pyrolytic graphite ($c = 6.708$ Å). The analysis of the data presented here is based on this method of determining λ_0.

B. The interferometer

The interferometer used in the experiments described in this paper is a considerably improved version of the same kind of device used in our early work.[2,3] It has been cut with a 600-grit, 4-in.-diameter, diamond blade from a 5-cm-dia-meter high-purity silicon perfect-single-crystal ingot. The room-temperature resistivity is ρ
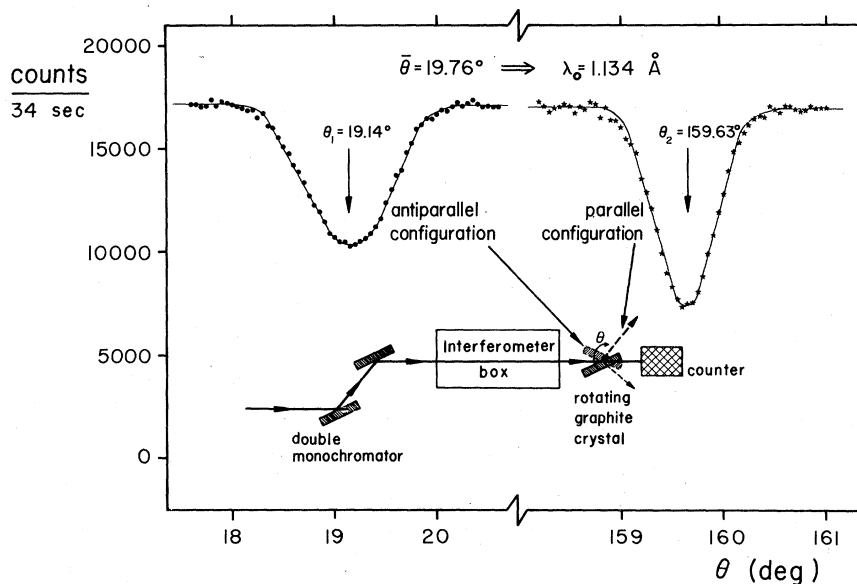
FIG. 5. An example of the method used to determine the neutron wavelength by measuring the angular spacing be-tween the transmission dips observed by rotating the pyrolitic graphite crystal in the beam transmitted through the interferometer.
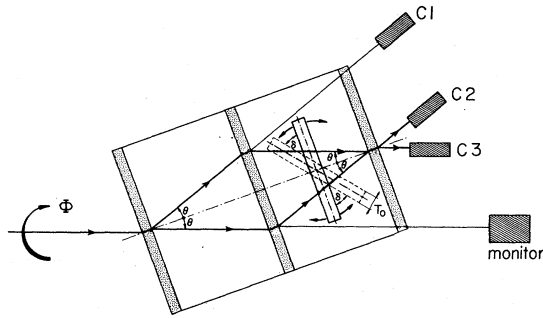
FIG. 6. Geometry of the Si-slab experiment shown in Fig. 7. The same geometry was used for the x-ray experiments designed to measure q_{bend} (Sec. V), in which case the Si slab is replaced by a plastic slab.

$= 3600$ ohm cm. The slab thickness is $a = 2.464 \pm 0.002$ mm, and the distance between the slabs is $d = 34.518 \pm 0.002$ mm. It has been found that most etchants for silicon do not leave the surfaces flat. In most cases, a surface originally flat comes out of the etch with a convex shape ("lens effect"). The departure from flatness due to this effect is enough in some cases to produce an appreciable phase shift across the beam dimensions. Although no silicon etchant is immune from this undesirable property, we found that some etchants work better than others. Our interferometer has been etched in a mixture of 3 parts HNO_3 (70%), 2 parts glacial acetic acid, and 1 part HF (30–40%) at room temperature for 3 min. The quality of our interfero-

meter can be seen from a measurement of the phase shift induced by the mean neutron-nuclear interaction potential. Placing a very flat, parallel slab of homogeneous material in the interferometer as shown in Fig. 6 and rotating it about an axis perpendicular to the interferometer scattering plane results in an oscillating counting rate in detectors C_2 and C_3. We show data obtained in this way for a Si slab (thickness $T = 0.2931$ cm) in Fig. 7. The slit size on the neutron beam was 8.2×3.6 mm^2. It is easy to show that the phase shift corresponding to a given rotation angle δ is

$$\beta_{shifter} = -2\lambda NbT \frac{\sin\delta \sin\theta_B}{\cos^2\theta_B - \sin^2\delta}, \qquad (19)$$

where N is the atom density, b the nuclear scattering length, θ_B the interferometer Bragg angle (220 planes), and λ the neutron wavelength. The period of these oscillations therefore provides a precision measurement of the scattering length b.

The experiments described in this paper have presented unusual difficulties with regard to mounting the interferometer. The experiments involve rotating the interferometer about a horizontal axis and also about a vertical axis. We have therefore been forced to find a method for holding the interferometer without straining it. We have tried a large selection of waxes, glues, and epoxies. In all cases the induced strain spoiled the performance of the interferometer. After considerable effort, we have discovered that
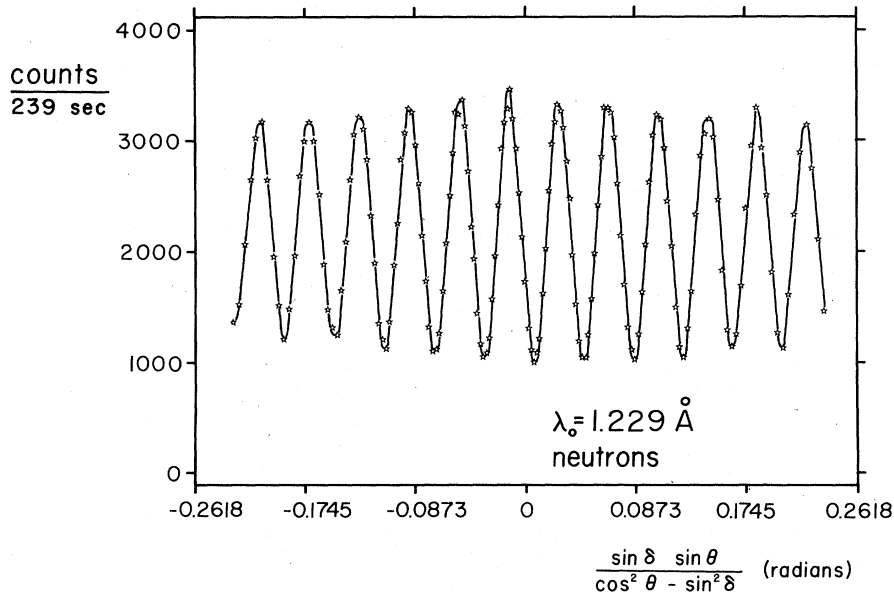
FIG. 7. Example of data obtained by rotating an Si slab in the interferometer (Fig. 6). The counts in detector C_3 are shown.

"double-sticky-back" plastic tape works. It provides the necessary adhesive character, yet it is sufficiently pliable and resilient so as to minimize the transmitted strain.

IV. THEORY OF THE EXPERIMENTS

Classically, the Hamiltonian governing a neutron's motion in the gravitational field of the rotating Earth is[18]

$$H = \frac{p^2}{2m_i} - G\frac{Mm_g}{r} - \vec{\omega}\cdot\vec{L}. \tag{20}$$

Here the angular momentum of the neutron's motion about the center of the Earth ($\vec{r}=0$),

$$\vec{L} = \vec{r}\times\vec{p}; \tag{21}$$

$\vec{p}$ is the canonical momentum of the neutron, $\vec{\omega}$ is the angular rotation velocity of the Earth, M the mass of the Earth, m_i the inertial mass of the neutron, and m_g the gravitational mass of the neutron. From an epistomological point of view, it is not possible to be confident that this Hamiltonian correctly describes quantum-mechanical phenomena, especially those involving interference. However, for lack of evidence to the contrary, we will assume it is also the correct quantum-mechanical Hamiltonian, and then see if the predictions based on it agree with the experiment. The principle of equivalence would require that the inertial mass m_i and the gravitation mass m_g in Eq. (20) are equal.

Since the distances involved within the neutron interferometer are very small compared to the radius R of the Earth, we can write (20) as

$$H = \frac{p^2}{2m_i} + m_g\vec{g}_0\cdot\vec{r} - \vec{\omega}\cdot\vec{L} + V_0, \tag{22}$$

where V_0 is the gravitational potential energy at some reference height above the Earth (say, the center of the interferometer), and $\vec{g}_0$ is the acceleration due to gravity. The classical equations of motion are Hamilton's equations

$$\dot{\vec{r}} = \frac{\partial H}{\partial \vec{p}}; \text{ and } \dot{\vec{p}} = -\frac{\partial H}{\partial \vec{r}}. \tag{23}$$

Here, the dot implies a time derivative, so that $\dot{\vec{r}}$ is the neutron velocity in the coordinate frame of the rotating Earth. The first of these equation gives the canonical momentum

$$\vec{p} = m_i\dot{\vec{r}} + m_i\vec{\omega}\times\vec{r}, \tag{24}$$

and the second gives its time derivative

$$\dot{\vec{p}} = m_g\vec{g}_0 - \vec{\omega}\times\vec{p}. \tag{25}$$

Combining Eqs. (24) and (25) we obtain the well-known equation of motion for a classical particle

in a rotating frame,

$$m_i\ddot{\vec{r}} = m_g\vec{g}_0 - m_i\vec{\omega}\times(\vec{\omega}\times\vec{r}) - 2m_i\vec{\omega}\times\dot{\vec{r}}. \tag{26}$$

Thus, the term $-\vec{\omega}\cdot\vec{L}$ in the Hamiltonian gives rise to both the centrifugal acceleration and the Coriolis acceleration. Since we will only be interested in the neutron's motion over distances corresponding to the dimensions of the interferometer, which are very small compared to the Earth's radius, we can define an effective gravitational acceleration in the usual way

$$\vec{g} = \vec{g}_0 + (m_i/m_g)\vec{\omega}\times(\vec{\omega}\times\vec{R}), \tag{27}$$

which we take to be independent of position $\vec{r}$. Under this assumption, we can solve (26) for the local motion of the neutron in the frame of the rotating Earth. To leading order in ω, the solution is

$$\vec{r} = \vec{r}_0 + \vec{v}_0 t + \tfrac{1}{2}(\vec{g}t^2) + \tfrac{1}{3}(\omega t^3 \vec{\omega}\times g). \tag{28}$$

The transit times for thermal neutrons through the interferometer in our experiments are of order 5×10^{-5} sec. Based on a sidereal day of 23 h, 56 min, one has $\omega = 7.29\times10^{-5}$ sec^{-1}. Thus, we see that the term in (28) involving ω is smaller than $\tfrac{1}{2}gt^2$ by a factor of about 10^{-9}. Therefore, the Coriolis force has a negligible effect on the trajectory over these small distances; however, its effect on the neutron phase is not negligible as we shall see.

The discussion so far has been based on classical mechanics. In order to calculate the phase shift β in a neutron interferometer experiment, we assume that we can associate a de Broglie wave of wave vector $\vec{k}$ with the neutron having canonical momentum $\vec{p}$:

$$\vec{p} = \hbar\vec{k}, \tag{29}$$

where $\hbar$ is Planck's constant divided by 2π. The phase difference for the neutron wave traversing the path ACD in Fig. 4 relative to the neutron wave traversing the path ABD is then given by

$$\beta = \frac{1}{\hbar}\int_{ACD}\vec{p}\cdot d\vec{r} - \frac{1}{\hbar}\int_{ABD}\vec{p}\cdot d\vec{r}$$

$$= \frac{1}{\hbar}\oint\vec{p}\cdot d\vec{r}. \tag{30}$$

The momentum appearing in this line integral on the path ACDBA around the interferometer is given by Eq. (24). The phase shift thus involves two terms,

$$\beta = \frac{m_i}{\hbar}\oint\dot{\vec{r}}\cdot d\vec{r} + \frac{m_i}{\hbar}\oint(\vec{\omega}\times\vec{r})\cdot d\vec{r}. \tag{31}$$

The velocity $\dot{\vec{r}}$ is obtained by differentiating Eq. (28). To a very high order of approximation we

can regard the trajectories between the interfero-
meter slabs as straight rather than parabolic
curves. The angular deviation, from a straight
line over these distances (for $\lambda = 1.4$ Å) is of
order 0.01″ of arc. It is fortunate that this angu-
lar deviation is about 10 times smaller than the
"Darwin acceptance width" for Bragg reflection
in the silicon crystals. If this were not so, a
neutron on the trajectory AB, say, would not be
Bragg reflected by the middle crystal slab of the
interferometer. The first term in (31), which we
will call β_{grav}, is the phase shift due to the gravi-
tational field of the Earth. To work out the inte-
gral for β_{grav} requires us to specify the direction
of the incident beam and the orientation angle ϕ
of the interferometer with respect to this direc-
tion (see Fig. 4). For a horizontally directed
incident beam the result is

$$\beta_{grav} = -2\pi m_i m_g (g/h^2)\lambda_0 A' \sin\phi \equiv -q_{grav} \sin\phi .$$

(32)

The area A' is given by

$$A' = (2d^2 + 2ad \cos\theta_B) \tan\theta_B .$$

(33)

The angle ϕ is defined to be zero when the plane
ABDC of the interferometer is horizontal. The
laboratory neutron wavelength is related to its
velocity by

$$\lambda_0 = h/m_i |\dot{\vec{r}}| ,$$

(34)

and θ_B is the Bragg angle. The result for a verti-
cally directed beam is given in Sec. VI.

The second term in Eq. (31), which we call
β_{Sagnac}, is due to the rotation of the Earth. Using
vector calculus, this integral is easy to evaluate,

$$\beta_{Sagnac} = \frac{4\pi m_i}{h} \vec{\omega} \cdot \vec{A} .$$

(35)

The normal area $\vec{A}$ enclosed by the beam paths is

$$A = (2d^2 + 2ad) \tan\theta_B .$$

(36)

The formula (35) was obtained by Page[19] using
wave-optical arguments, and by Anandan[20] and
Stodolsky[21] within the framework of general rela-
tivity. Recently, an interesting derivation has
been given by Dresden and Yang[22] in which the
phase shift for either a rotating neutron or optical
interferometer is derived from the point of view
of a Doppler shift due to a moving source and
moving reflecting crystals.

The actual path of any given neutron within a
crystal slab is more complicated than the line
drawn straight across the crystal as shown in
Fig. 1. There is a current $\vec{j}_\alpha$ carried by the α-
branch part of the wave function and a current $\vec{j}_\beta$
carried by the β-branch part of the wave func-

tion. In addition, there is a current $\vec{j}_{\alpha\beta}$ due to
the interference of the α- and β-branch wave func-
tions which leads to a sinusoidal trajectory for
the neutron. This is the phenomenon which leads
to Pendellösung interference fringes. Considera-
tion of these effects has recently been treated in
extensive detail by one of us.[23] The conclusion
reached is that to very high order of approxima-
tion the trajectory can be regarded as a straight
line across the crystal, and that the microscopic
details of the trajectory do not play a role in cal-
culating the net phase shift due to gravity within
the crystal medium.

V. GRAVITATIONALLY INDUCED QUANTUM INTERFERENCE

In this section we will confine our attention to
experiments in which a horizontally directed inci-
dent beam is utilized as shown in Fig. 4. The
experimental procedure involves turning the
interferometer, including the entrance slit and the
three detectors C_1, C_2, and C_3, about the incident
beam line AB. At each angular setting ϕ, neu-
trons are counted for a preset length of time
(actually based on the incident beam monitor).
This procedure allows the neutron on the beam
trajectory CD to be somewhat higher above the
surface of the Earth than for the beam path AB.
The difference in the Earth's gravitational poten-
tial between these two levels causes a quantum-
mechanical phase shift of the neutron on the tra-
jectory ACD relative to the trajectory ABD. The
phase shift on the rising path AC is exactly equal
to the phase shift on the opposite rising path BD,
as can be shown by applying Huygen's principle.

The phase shift β_{grav} depends on the product of
the inertial and gravitational masses $m_i m_g$ of the
neutron. Thus, measuring this phase shift in-
duced by the Earth's gravity can be regarded as
a test of the princple of equivalence in the quan-
tum limit if we compare the mass

$$m_n = (m_i m_g)^{1/2}$$

(37)

with the neutron mass obtained from mass spec-
troscopy results on the proton and the deuteron
according to the formula

$$m_n = m_D - m_p + E_\gamma /c^2 = 1.6747 \times 10^{-24} \text{ g} .$$

(38)

The deuteron binding energy is obtained from the
radiative capture gamma-ray energy E_γ (=2.23
MeV). The fact that this experiment is a test in
the quantum limit is apparent since quantum-
mechanical interference is involved, and Planck's
constant appears explicitly in the formula (32).

A. The total phase shift

Unfortunately, as we have pointed out previously,[2] there is an additional effect on the measured phase shift β resulting from bending (or warping) of the interferometer under its own weight. This effect is dependent upon the rotation angle ϕ, since the experiment involves turning the interferometer about an axis which is not an axis of elastic symmetry. We call this effect

$$\beta_{\text{bend}} = -q_{\text{bend}} \sin\phi . \qquad (39)$$

In Subsec. B below we will justify writing β_{bend} in this form.

For a horizontally directed incident beam we can easily work out the dot product involved in evaluating β_{Sagnac} in Eq. (35); the result is

$$\beta_{\text{Sagnac}} = \frac{4\pi m_i}{h} \omega A (\cos\phi \cos\theta_L + \sin\phi \sin\Gamma \sin\theta_L) , \qquad (40)$$

where θ_L is the colatitude angle, Γ is the angle of the incident neutron beam west of due south. Beam port B is oriented nearly exactly along a north-south line, such that the monochromatic beam incident on the interferometer is directed due south. Thus, the angle Γ in Eq. (40) is zero for our experiments, and we can write (40) in the form

$$\beta_{\text{Sagnac}} = q_{\text{Sagnac}} \cos\phi , \qquad (41)$$

where

$$q_{\text{Sagnac}} = (4\pi m_i \omega A/h) \cos\theta_L . \qquad (42)$$

Consequently, the total phase shift in these experiments involves three contributions

$$\beta = \beta_{\text{grav}} + \beta_{\text{Sagnac}} + \beta_{\text{bend}}$$

$$= -q_{\text{grav}} \sin\phi + q_{\text{Sagnac}} \cos\phi - q_{\text{bend}} \sin\phi . \qquad (43)$$

We see that the Sagnac effect is maximum for ϕ

$= 0°$, while the gravity and bending effects are maximum for $\phi = 90°$. We can rewrite Eq. (43) as

$$\beta = q \sin(\phi - \phi_0) , \qquad (44)$$

where

$$q^2 = (q_{\text{grav}} + q_{\text{bend}})^2 + q_{\text{Sagnac}}^2 \qquad (45)$$

and

$$\tan\phi_0 = \frac{q_{\text{Sagnac}}}{q_{\text{grav}} + q_{\text{bend}}} . \qquad (46)$$

The fact that the phase shift due to the Earth's rotation (Sagnac effect) depends upon $\cos\phi$ and not $\sin\phi$ comes about as a result of our selection of due south as the incident beam direction [$\Gamma = 0$ in Eq. (40)]. This leads to an important experimental circumstance. Although q_{Sagnac} is of order 2.5% of q_{grav}, its contribution to the total frequency of oscillation q of the interference pattern is very small (of order 3 parts in 10^4). However, it leads directly to a shift ϕ_0 in the center of the interference pattern. Table I gives the calculated wavelength dependence of q_{grav}, q_{Sagnac}, and ϕ_0. We have used the colatitude angle $\theta_L = 51.37^0$ and the acceleration due to gravity $q = 980.0$ cm/sec^2 at Columbia, Missouri, along with the dimensions of our interferometer given in Sec. III to compile this table.

B. Bending

The values for q_{bend} given in Table I have been obtained from a series of experiments using x rays. The procedure involves using molybdenum $K\alpha$ x rays ($\lambda = 0.71$ Å). We direct a beam of x rays along the same incident line AB (Fig. 4) and observe the interfering x-ray beams with an x-ray sensitive porportional gas detector as a function of rotation angle ϕ. The effect of gravity (gravitational red shift) on the x rays over the

TABLE I. Calculated frequencies of oscillation, q.

λ_0 (Å)	θ_B (deg)	A (cm^2)	A' (cm^2)	q_{grav} (radians)	q_{Sagnac} (radians)	q_{bend} (radians)	θ_0 (deg)
0.6	8.9885	4.038 56	4.035 25	9.5255	0.582 396	1.406 41	3.297 62
0.8	12.0236	5.437 91	5.429 97	17.0904	0.784 196	1.875 21	2.512 07
1.0	15.0934	6.885 82	6.869 99	27.0285	0.992 997	2.344 01	2.029 54
1.2	18.2083	8.398 46	8.370 45	39.5181	1.211 13	2.812 82	1.703 26
1.4	21.3800	9.995 43	9.949 61	54.8024	1.441 43	3.281 62	1.468 07
1.6	24.6220	11.7011	11.630 3	73.2109	1.687 41	3.750 42	1.290 62
1.8	27.9505	13.5471	13.441 8	95.1913	1.953 62	4.219 23	1.152 08
2.0	31.3851	15.575 4	15.423 6	121.362	2.246 12	4.688 03	1.041 03
2.2	34.9503	17.844 5	17.630 1	152.596	2.573 33	5.156 83	0.950 109
2.4	38.6781	20.438 7	20.140 0	190.168	2.947 44	5.625 63	0.874 415
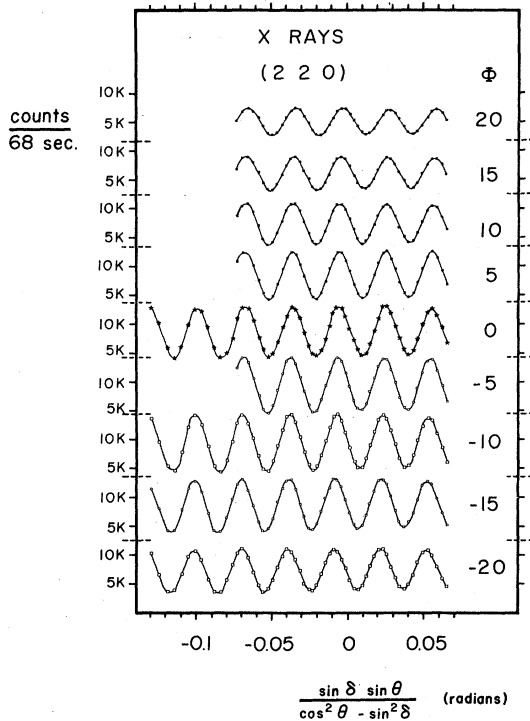
FIG. 8. X-ray (Mo $K\alpha$) intensity as a function of the plastic-slab orientation angle δ (see Fig. 6) for various settings ϕ of the interferometer. This data is for the (220) reflection in Si. The shift of phase Δ of this data as a function of ϕ is used to determine q_{bend}.

distances involved in the interferometer is negligible. The x-ray Sagnac effect is also negligible. Because the x-ray wave field may not remain totally uniform (coherent) over the cross section of the interfering beams (due to warping of the three interferometer slabs), a plot of intensity vs ϕ will not necessarily give q_{bend} exactly. In addition, due to extreme care in the methods we use to mount the interferometer, q_{bend} is fairly small, and we do not observe a complete oscillation period for the range of rotation angles ϕ utilized. We circumvent these problems by measuring the shift in the phase of an interference oscillation pattern resulting from rotation of a very flat slab of plastic in the interferometer (see Fig. 6 for the geometry) as a function of the angle ϕ. Data obtained in this way are shown in Fig. 8 in which Mo$K\alpha$ x rays were reflected by the (220) planes in the interferometer. We have obtained a similar set of data for the (440) reflection as shown in Fig. 9. The results of these experiments are shown in Fig. 10 where we plot the shift of phase of the plastic slab oscillation pattern Δ vs $\sin\phi$. We observe a linear relation which justifies the form of Eq. (39). The slope of these plots gives q_{bend}. It is reasonably cer-
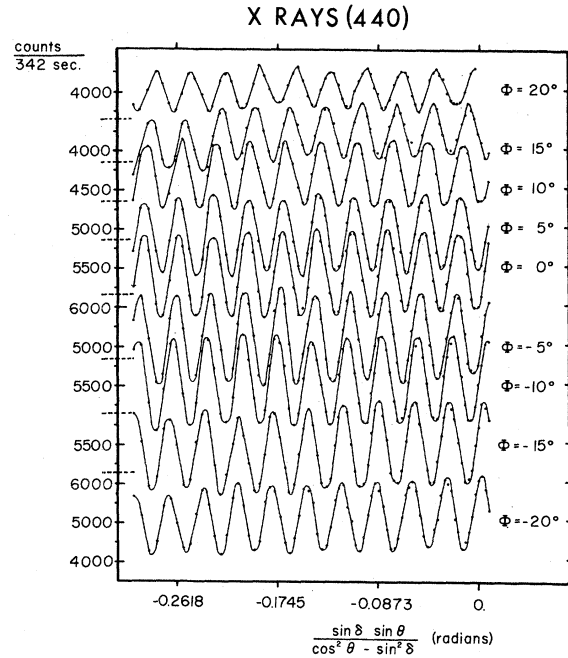
FIG. 9. X-ray data for the (440) reflection in Si.

tain that the functional form of the phase shift must be

$$\beta_{bend} = k\Delta d = (2\pi/\lambda_0)\Delta d, \tag{47}$$

where Δd is the difference in path length for the trajectory ABD relative to ACD due to bending of the interferometer. From the fact that the slope of the (440) data is very nearly four times the
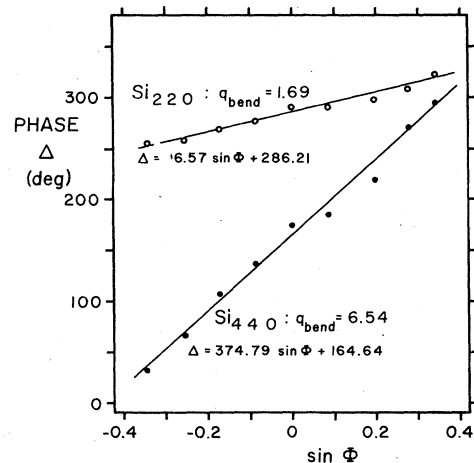
FIG. 10. A plot of the phase shift Δ of the interference oscillations resulting from rotating a plastic slab (Fig. 6) in the interfering x-ray beams for various angles ϕ. The two sets of data are for reflecting Mo $(K\alpha)$ x rays (0.71 Å) from the (220) and (440) planes in Si. The slope of these plots gives q_{bend}.
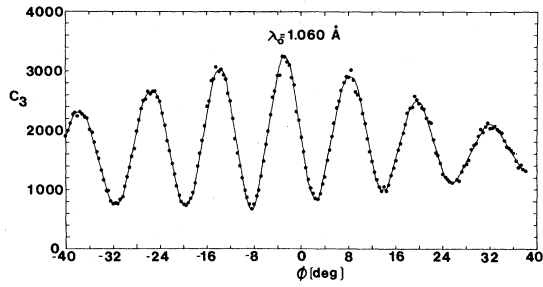
FIG. 11. Gravitationally induced quantum interference experiment at $\lambda_0 = 1.060$ Å. The counting time was about 5 min per point.

slope of the (220) data, we conclude that

$$\Delta d \propto \sin^2 \theta_B . \tag{48}$$

Therefore putting the arguments together that have led to (39), (47), and (48) we find

$$\beta_{\text{bend}} = -q_{\text{bend}} \sin\phi = -(C/\lambda_0) \sin^2\theta_B \sin\phi ; \tag{49}$$

the numerical value of the constant C from the data is

$$C = 34.57 \text{ rad Å} . \tag{50}$$

The reason why the bending effect seems to depend quadratically on $\sin\theta_B$ is not yet understood.

C. Experimental results

We show in Figs. 11 and 12 representative data obtained at two wavelengths: $\lambda_0 = 1.060$ and 1.419 Å, respectively. The neutron counting rate in detector C_3 is plotted versus the interferometer rotation angle ϕ. The contrast (maximum/minimum) of these data is seen to be about 3 to 1. Contrasts as high as 8 to 1 have been observed in some runs. To obtain the frequency of oscillation q we Fourier transform the data numerically according to

$$F_q = \sum_{j=1}^{N} I(\sin\phi_j) e^{iq \sin\phi_j} , \tag{51}$$

where I is the oscillatory part of the neutron in-
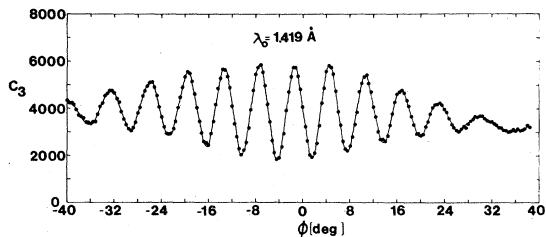
FIG. 12. Gravitationally induced quantum interference experiment at $\lambda_0 = 1.419$ Å. The counting time was about 7 min per point.
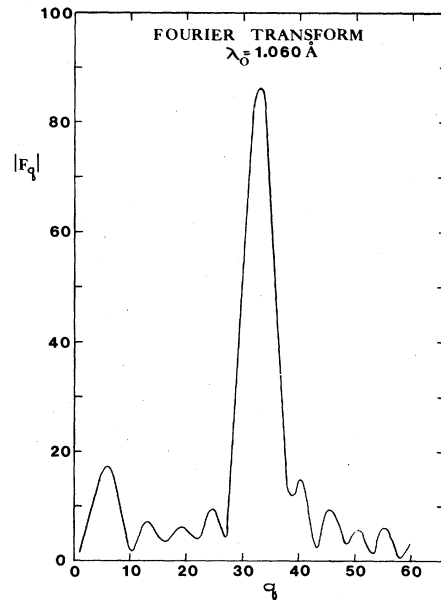
FIG. 13. Fourier transform of the data of Fig. 11.

tensity, and the index j runs over all N datum points. The Fourier transforms of the data of Figs. 11 and 12 are shown in Figs. 13 and 14.

There is loss of contrast at larger rotation angles ϕ, which we believe to be due to warping of the interferometer under its own weight as the interferometer is rotated. This explanation of the effect is in accord with various experiments we have carried out with reduced slit sizes in which the loss of contrast is reduced. We have found that as the neutron wavelength becomes larger the loss of the contrast occurs at smaller rotation angles ϕ. This observation is also in agreement with the above explanation, since the bending effect measured with x rays is proportional to $\sin^2\theta_B (= \lambda_0^2 G^2/4)$.

In any interferometry experiment, the long-term
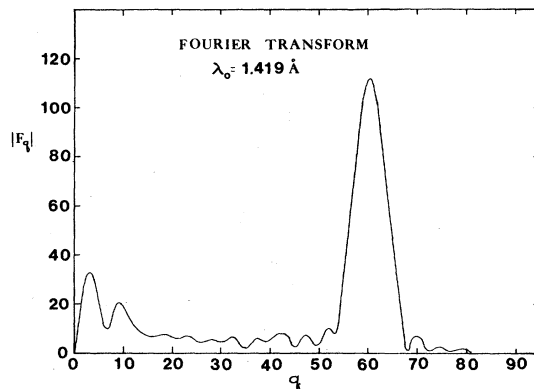
FIG. 14. Fourier transform of the data of Fig. 12.

$\lambda_0 = 1.05$ Å

data taken from
- 38.4 to -41.6 deg
- 32 " -38.4 "
- 26 " -32.4 "
- 26 " -26.4 "
- 20 " -20.4 "
- mean value
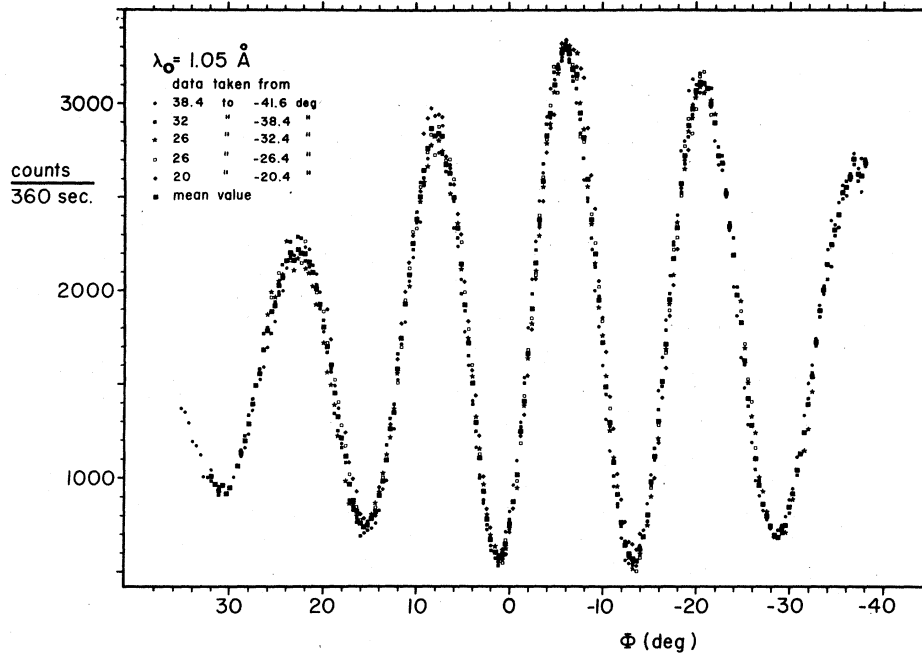
FIG. 15. Gravitationally induced quantum interference experiment at $\lambda_0 = 1.050$ Å. These are data from 6 runs taken over a period of about 75 h. These data show the long-term phase stability of the interferometer.

phase stability is an important consideration. We show in Fig. 15 data obtained at $\lambda_0 = 1.050$ Å in which we have tested the phase stability of our interferometer. This figure shows the gravita-

FIG. 16. A plot of the frequency of oscillation of q of a large series of scans of the type shown in Figs. 11 and 12 as a function of wavelength λ_0. The dashed curve is the least-squares fit to the data using Eqs. (32) and (49). The labels next to the data points are run numbers.

tionally induced quantum interference fringes obtained on 5 separate runs. The total data collection time was about 75 h. We see that the phase stability over this period of time is extremely good. The fact that the interferometer is mounted inside a heavy aluminum box, which in turn is mounted inside a large heavy masonite neutron shield, creates isothermal conditions sufficient to obtain data of this quality.

We have now taken data of the type shown in Figs. 11 and 12 at a wide selection of neutron wavelengths. The frequency of oscillation q for each run has been obtained both by the Fourier-transform method discussed above and by a least-squares-fitting procedure (which is discussed in the next section). These two data analysis techniques agree to within the statistical uncertainty of the raw data. The results of this extensive set of measurements is summarized in Fig. 16 in which we have plotted the observed frequency of oscillation q versus the incident neutron wavelength λ_0. The dashed line is the prediction of theory, based on Eq. (32) and the measured frequency of oscillation due to bending. We have fitted the theoretical curve to the data leaving $(m_i m_g)^{1/2}$ as an adjustable parameter. We find

$$(m_i m_g)^{1/2} = (1.675 \pm 0.003) \times 10^{-24} \text{ g} \qquad (52)$$

which agrees with the rest mass of the neutron obtained from mass spectroscopy to within the limits of error.

VI. NEUTRON SAGNAC EFFECT

We pointed out in the previous section that the contribution of q_{Sagnac} to the total frequency of oscillation of the interference pattern is very small as a result of our selection of the direction of the incident neutron beam. However, the Sagnac effect leads to an angular shift ϕ_0 in the center of the interference pattern given by Eq. (46). In Subsec. A we will discuss our results on the measurement of ϕ_0. We have also pursued an alternative approach, utilizing a vertically directed incident beam, to observe the neutron Sagnac effect. These experiments are described in Subsec. B.

A. Horizontal-incident-beam experiments

According to Eqs. (2) and (44) the counting rate in detector C_3 should vary with the rotation angle ϕ according to the formula

$$I_3(\phi) = \alpha\{1 + \cos[q \sin(\phi - \phi_0) + \beta_0]\}, \tag{53}$$

where β_0 is the "zero-phase" of the interferometer resulting from the fact that the two legs ABD and ACD are not precisely equal. It is apparent that in order to separately measure ϕ_0 and β_0, data must be accumulated over an angular range of $(\phi - \phi_0)$ where the sine function departs from linearity.

This presents special difficulties since the warping of the interferometer at large ϕ tends to wash out the contrast. Because of this loss of contrast the analytical form of the intensity $I_3(\phi)$ is more complicated than Eq. (53). We have pursued this problem by a least-squares fitting procedure in which we use a parametrized form of the intensity profile. Since the experimental results of the type shown in Figs. 11 and 12 exhibit an envelope and a weakly sloping mean level, we have chosen the form

$$I_3(\phi) = A + B\phi + C\phi^2$$
$$+ D \cos[Q \sin\phi + \Delta_1] \cos[q \sin(\phi - \phi_0) + \beta_0]$$
$$\tag{54}$$

as a phenomenological generalization of Eq. (53). There are nine parameters in this equation: A, B, C, D, Q, Δ_1, β_0, q, and ϕ_0. We are, of course, only interested in q and ϕ_0. The results of an extensive series of measurements and data analyses are shown in Fig. 17. The dashed line is the result of a numerical calculation based on Eq. (46) relating the angle ϕ_0 to q_{Sagnac}. Since q_{Sagnac} is independent of wavelength (aside from its dependence on the area A), and q_{grav} is proportional to the wavelength (aside from its dependence on the area A'), we see that except for the small correc-
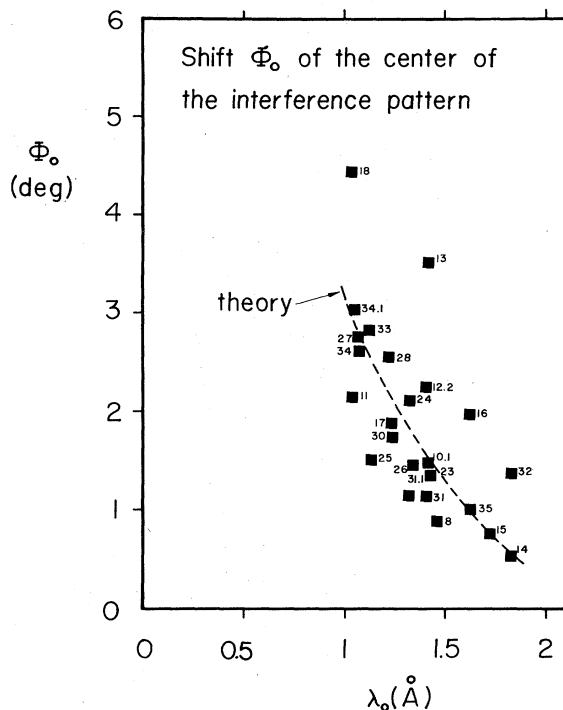
FIG. 17. Experimental results for the shift ϕ_0 of the center of the interference patterns as a function of wavelength λ_0. These results were obtained by least-squares fitting of the functional form of Eq. (54) to a large series of data of the type shown in Figs. 11 and 12. The angle ϕ_0 is related to the frequency of oscillation due to the neutron Sagnac effect as given by Eq. (46). The dashed curve labeled "theory" is the result of using Eq. (46) and the geometric parameters of the interferometer given in the text. The labels next to the data points are run numbers.

tion due to q_{bend} in Eq. (46), ϕ_0 should be inversely proportional to λ_0. From this data it is clear that we are observing the neutron Sagnac effect. However, the scatter in the data is rather severe.

B. Vertical-incident-beam experiments

We show in Fig. 18 a schematic diagram of our most recent experiments designed to detect the neutron Sagnac effect. The initially horizontal beam from the monochromator is reflected by a beryllium crystal through 90°, such that the beam incident on the interferometer is vertical (along a plumb line). The experimental procedure involves turning the interferometer about the vertical line AB through various angular settings ϕ. For a beam which is precisely vertical, the phase shift due to gravity, β_{grav}, is independent of the angle ϕ, as can be seen from symmetry. However, the angle between the rotation axis $\vec{\omega}$ of Earth and the interferometer normal area vector $\vec{A}$ is ϕ dependent. Thus, this incident beam orientation allows
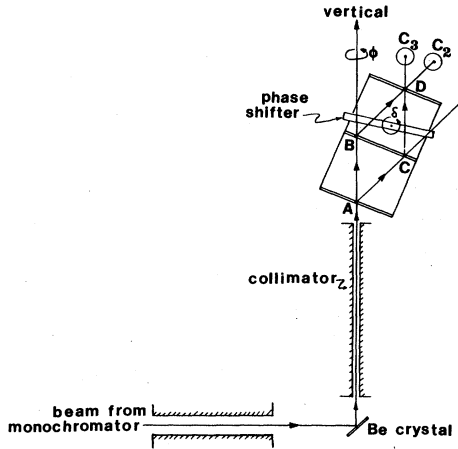
FIG. 18. Schematic diagram of the configuration of
the apparatus for the vertical-beam experiments de-
signed to measure the neutron Sagnac effect. The draw-
ing is not to scale. The collimator is approximately
1 m in length, and the interferometer is approximately
8 cm long from point A to point D. The angle δ of the
phase shifter is defined to be zero when it is parallel
to the three interferometer slabs.

us to experimentally suppress the effects of gra-
vity, leaving only the effect of the rotation of the
Earth on the phase shift. The bending effect is
also independent of ϕ since the orientation of the
interferometer with respect to $\vec{g}$ is fixed. The
suggestion that the Sagnac effect could be obser-
ved with this geometry was first made by Anan-
dan.[20]

Using Eq. (35) it is an easy matter to work out
the formula for β_{Sagnac} as a function of ϕ; we get

$$\beta_{\text{Sagnac}} = (4\pi m_i/h)\omega A \sin\phi_L \sin\phi$$

$$= q^v_{\text{Sagnac}} \sin\phi . \tag{55}$$

The superscript "v" indicates that this expression
is for a vertically directed incident beam. For
these experiments the incident wavelength is fixed
at $\lambda_0 = 1.262$ Å, which in turn determines the value
of the normal area, which is $A = 8.864$ cm^2. The
angle ϕ is defined to be zero, when the normal
area vector $\vec{A}$ is directed due west. The predicted
frequency of oscillation is

$$q^v_{\text{S agnac}} = 91.92 \text{ deg} = 1.604 \text{ rad.} \quad \text{(theory)}. \tag{56}$$

As we turn the interferometer through various
angles ϕ, the counting rate is expected to vary
according to

$$f(\phi) = A + B \cos(q^v_{\text{Sagnac}} \sin\phi + \beta_0) . \tag{57}$$

By allowing A and B to be numerically different,
we have taken into account the fact that perfect
contrast is never actually realized in practice.
The results of such an experiment are shown in
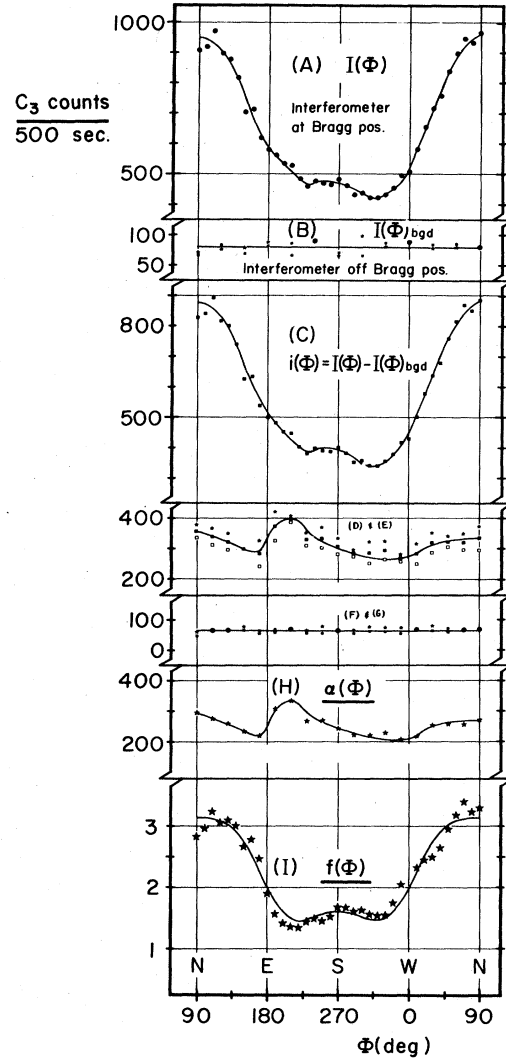
FIG. 19. Data taken in a "direct" measurement of the
effect of the Earth's rotation on the neutron phase snift.
The various parts of this figure are explained in detail
in Sec. VIB.

Fig. 19. There is a difficulty in directly inter-
preting the counting rate in detector C_3 to be $f(\phi)$.
There is a natural variation of the "effective"
incident beam intensity which is the angular ac-
ceptance range for Bragg scattering by the silicon
interferometer. This is due to the energy-angle
correlations in the incident beam resulting from
the monochromation process using single crystals.
However, one can measure this variation sepa-
rately by blocking off the beam in one leg of the
interferometer (and then the other) and measuring
the effective beam strengths under noninterfering
conditions. The series of curves in Fig. 19 are
the results of utilizing this idea. Part (A) of this
figure is the raw data for the counting rate in de-

tector C_3 versus ϕ. Part (B) is the background
counting rate with the interferometer rotated off
the Bragg reflecting condition. Part (C) is the
raw data minus the background, which we call
$i(\phi)$. The sets of data (D) and (E) are the counting
rates in detector C_3 when beam I is blocked off
and then beam II is blocked off with a cadmium
absorber. Parts (F) and (G) are the background
counting rates under these conditions. Part (H)
gives the average of the data in scans (D) and (E)
minus the average background of scans (E) and
(G). The data of part (H), called $\alpha(\phi)$, is directly
proportional to the effective incident beam inten-
sity. The final graph, part (I), is obtained by
dividing $i(\phi)$ in part (C) by $\alpha(\phi)$ in part (H), that
is,

$$f(\phi) = i(\phi)/\alpha(\phi). \tag{58}$$

This procedure allows us to divide out the angle-
energy correlation effects, leaving only variations
with ϕ due to interference. The solid line in part
(H) is a least-squares fit of the data to the func-
tional form (57). We find

$$q_{S_{agnac}}^v = 104.4 \pm 0.4 \text{ deg}$$

$$= 1.822 \pm 0.007 \text{ rad (expt.)}. \tag{59}$$

This value is to be compared with 91.92 deg in Eq.
(56). There are several difficulties with this tech-
nique. The most serious one is that it involves
a number of independent steps in the sequence in
arriving at the corrected plot in part (I). Thus,
the experimental systematic and statistical errors
accumulate.

In order to circumvent this difficulty we have
developed a technique in which we directly mea-
sure the phase shift. We insert a slab-shaped
phase shifter into the interferometer as shown in
Fig. 18. This slab is, in fact, another Si single
crystal of thickness $T = 0.2931$ cm, although it
could be made of any material. Rotating this slab
through an angle δ about an axis normal to the
parallelogram ABDC results in a phase shift aris-
ing from the mean neutron-nuclear potential. The
formula for this phase shift was given in Sec. III,
Eq. (19). As we rotate this phase shifter through
various angles δ, the counting ratios in detectors
C_2 and C_3 are observed to oscillate. Repeating
this procedure at another setting ϕ of the inter-
ferometer results in another oscillating pattern,
of the same period, but shifted in phase with re-
spect to the first pattern. We show in Fig. 20(a)
data taken at $\phi = 0°$ and in Fig. 20(b) data taken
at $\phi = -90°$. The phase shift between these two
patterns is due to the rotation of the Earth. The
results of an extensive series of measurements
are shown in Fig. 21. Each datum point in this
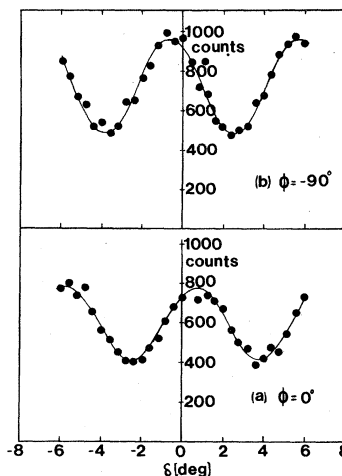
FIG. 20. Typical oscillating counting rates observed
in detector C_3 at two orientation settings ϕ of the inter-
ferometer. The counting time for each datum point was
approximately 600 sec.

figure was obtained by least-squares fitting of a
sine wave of unknown phase to data of the type
shown in Fig. 20. Because of long-term drifts
of the interferometer phase, measurements at a
reference angle (usually $\vec{A}$ pointing east or west)
were repeated after each new setting ϕ.

The labeling of north, south, east, and west on
this diagram was achieved through an astronomi-
cal sighting of the star Polaris. This line of sight
was carried inside the reactor hall (which is be-
low ground level) by precision surveying techni-
ques and transferred onto the interferometer with
a laser mounted on a rotary table.

The solid curve in Fig. 21 is the result of a
least-squares fitting of the data to a sine wave.
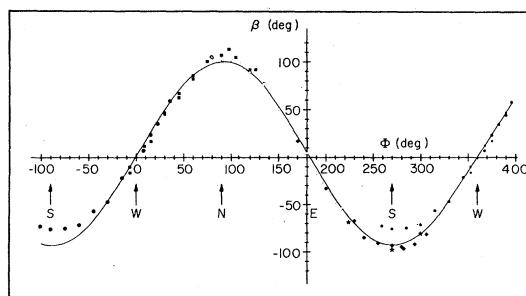
FIG. 21. A plot of the phase shift β due to the Earth's
rotation as a function of orientation ϕ of the normal
area $\vec{A}$ of the interferometer about a vertical axis. The
symbols N, W, S, and E indicate north, west, south,
and east. These data were taken in six sections as dis-
cussed in the text. The different symbols are for the
interferometer box facing various directions.

It gives

$$q^v_{\text{Sagnac}} = 96.8 \pm 0.2 \text{ deg}$$

$$= 1.689 \pm 0.003 \text{ rad (expt).} \quad (60)$$

This result is in closer agreement with theory than the result (59). However, it is obvious from the data that there is still a substantial problem. These data were taken in six steps. Because of geometrical limitations of the rotator inside the heavy masonite shield, we were only able to accumulate data over an angular range of ϕ of about 130°. To obtain data through other ranges of ϕ it was necessary to turn the entire masonite shield box through large angles (typically 90°). This required releveling and orienting of the rotator assembly. One notes that the data from each of the six sequences do not fit perfectly together. This fact points up the need for extreme care and precision in this experiment. Since the magnitude of the frequency of oscillation due to gravity is about 50 times the frequency due to the Earth's rotation, a small misalignment of the beam axis off verticality results in a contribution from β_{grav}. If the incident beam is off the axis of a plumb line by an angle γ, the ϕ-dependent part of the phase shift due to gravity is

$$\beta_{\text{grav}} = q_{\text{grav}} \sin\phi \sin\gamma, \quad (61)$$

where q_{grav} is given in Sec. IV. To give an idea of the size of the effect, suppose $\gamma = 0.1°$. At $\lambda_0 = 1.262$ Å, $q_{\text{grav}} = 44$ deg rad $= 2521$ deg, giving $\beta_{\text{grav}} = 4.4$ deg. Thus, a misalignment of the axis of the beam (and also the axis of rotation) of 0.1° will result in an error of about 5% in the measurement of the neutron Sagnac effect. On the basis of these considerations, we now feel that the unusual agreement of experiment with theory reported in our preliminary paper was somewhat fortuitous.

We have now modified the heavy masonite shield so that the rotator assembly can be turned through a full 360 deg without realigning the beam axis. We have exercised extreme care in aligning the beam axis using precision levels. Our most recent data taken under these conditions are shown in Fig. 22. The solid curve is again a least-squares fitting of this data to a sine curve. We find

$$q^v_{\text{grav}} = 94.6 \pm 0.3 \text{ deg}$$

$$= 1.651 \pm 0.005 \text{ rad (expt).} \quad (62)$$

This result is within 3% of the theoretical prediction (56). We believe that to improve upon this result would require new techniques, of which we are not aware.
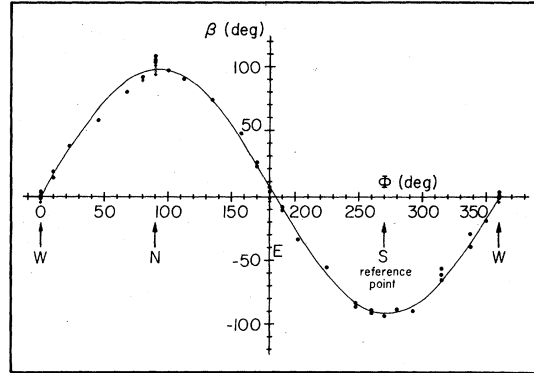
FIG. 22. A plot of the phase shift β due to the Earth's rotation as a function of orientation ϕ as in Fig. 21. These data were taken after modification of the rotator assembly to allow a complete 360° sequence of scans to be performed without realignment of the verticality of the incident beam.

VII. CONCLUSIONS

Our observation of quantum-mechanical interference phenomena in these experiments confirms that the Newtonian potential $m\vec{g} \cdot \vec{r}$ must be included in Schrödinger's equation, and that this potential influences the *phase* of the neutron wave function in a manner expected for any other potential. We believe that this result has a fairly deep significance which concerns the principle of equivalence.

The equality of inertial and gravitational mass is one statement of this principle. The classical experiments[11] of Eötvös and Dicke have verified this equality to very high precision. An alternative and stronger statement of this princple requires that the results of an experiment carried out in a uniform gravitational field cannot be distinguished from the results of an experiment carried out in a gravity-free laboratory experiencing a constant acceleration.

All verifications of the equivalence principle, prior to our experiment, have been in the classical domain. The experimental results did not depend on Planck's constant. For the experiments described in this paper, the number of interference fringes observed for a given rotation of the interferometer depends on the numerical value of Planck's constant, and therefore represent a test of the principle of equivalence in the *quantum limit*.

Since the phase shifts observed in our gravitationally induced quantum-interference experiment depend upon the product $m_i m_g$, and the phase shifts in the Sagnac experiment depend only on m_i, we can certainly claim that the combination of these experiments demonstrates the equivalence of inertial and gravitational mass in a quantum-

mechanical phenomenon. We would like to propose that a stronger and deeper conclusion can be reached.

In order to truly verify the principle of equivalence one must carry out two experiments—one on the surface of the Earth in a laboratory at rest, and another in a laboratory far out in space having an acceleration g. We have not done this experiment. However, we suggest that the second experiment need not be done if one accepts the validity of Schrödinger's equation in a gravity-free, inertial frame. If this is granted, then the outcome of an interferometer experiment in an accelerated laboratory can be calculated with certainty. This has been done,[12] and we find that the observed phase shift in our Earth-bound experiment agrees with this prediction if we replace the laboratory acceleration a with g in the final formula.

To summarize then, one must either question the validity of Schrödinger's equation under zero-gravity conditions or assert that we have verified the stronger statement of the equivalence principle in the quantum limit. The first alternative seems unacceptable.

It would be very exciting to carry out these experiments at both very low neutron energies and at very high neutron energies. In the ultra-cold neutron energy region where the change in gravitation potential energy is comparable to the neutron kinetic energy, the WKB approximation for calculating phase shifts fails and the neutron trajectory is not well defined. In the very high neutron energy region where terms of order $(v/c)^2$ cannot be neglected one will begin to see general relativistic effects as discussed by Anandan[20] and Stodolsky.[21] We believe that experiments in both regions of neutron energy are possible, and we are currently pursuing certain new ideas along these lines.

ACKNOWLEDGMENTS

APPENDIX A: DYNAMICAL THEORY OF NEUTRON DIFFRACTION

We review here the essential aspects of the dynamical theory of diffraction for the symmetrical Laue-transmission geometry (Fig. 23). For further details we refer the reader to various review articles.[24-26] We assume that the absorption is zero, which is a very good approximation for silicon.

Let the incident-neutron wave function be given by the plane wave

$$\phi(r) = \Phi \exp(i\vec{k}_0 \cdot \vec{r}) . \tag{A1}$$

To find the wave function $\psi(\vec{r})$ inside the crystal, we must solve the Schrödinger equation

$$[-(\hbar^2/2m)\nabla^2 + V(\vec{r})]\psi = E_0\psi , \tag{A2}$$

where $V(\vec{r})$ is the periodic interaction potential of the neutron with the lattice. Defining

$$v(\vec{r}) \equiv (2m/\hbar^2)V(\vec{r}) \tag{A3}$$

and

$$k_0^2 \equiv (2m/\hbar^2)E_0 , \tag{A4}$$

Eq. (A2) can be written as

$$(\nabla^2 + k_0^2)\psi = v\psi . \tag{A5}$$

We now write $\psi(\vec{r})$ as a Bloch function

$$\psi(\vec{r}) = \sum_{\vec{G}} \psi_{\vec{G}} \exp(i\vec{k}_0 \cdot \vec{r} + i\vec{G} \cdot \vec{r}) , \tag{A6}$$

and expand $v(\vec{r})$ in the Fourier series

$$v(\vec{r}) = \sum_{\vec{G}} v_{\vec{G}} e^{i\vec{G} \cdot \vec{r}} . \tag{A7}$$

The vectors $\vec{G}$ are the reciprocal lattice vectors of the crystal. Putting (A6) and (A7) into the wave equation (A5) and equating coefficients of $e^{i\vec{G}' \cdot \vec{r}}$, we find

$$\psi_{\vec{G}'}[k_0^2 - (\vec{K}_0 + \vec{G}')^2] = \sum_{\vec{G}''} v_{\vec{G}'-\vec{G}''}\psi_{\vec{G}''} . \tag{A8}$$
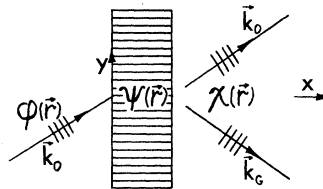
FIG. 23. Schematic diagram of the symmetric Laue geometry. ϕ is the incident plane wave. ψ is the wave function inside the crystal and χ is the wave function emerging from the back face of the crystal.

We now make an approximation. We assume that $\vec{k}_0$ is oriented very close to the Bragg condition for a particular reciprocal lattice vector $\vec{G}$, and assume that the internal incident wave vector $K_0 \approx k_0$, as we can easily verify. Thus, the "resonance factor" $[k_0^2 - (\vec{K}_0 + \vec{G}')^2]$ is small only for $\vec{G}' = \vec{G}$ and for $\vec{G}' = 0$. That is, only ψ_0 and $\psi_{\vec{G}}$ will be large. Under these conditions, the above infinite set of equations reduces to two equations; in matrix form they are given by

$$\begin{bmatrix} (K^2 - K_0^2) & -v_{-\vec{G}} \\ -v_{\vec{G}} & (K^2 - K_G^2) \end{bmatrix} \cdot \begin{bmatrix} \psi_0 \\ \psi_{\vec{G}} \end{bmatrix} = 0, \qquad \text{(A9)}$$

where we have defined

$$K^2 \equiv k_0^2 - v_0 \qquad \text{(A10)}$$

and

$$\vec{K}_G = \vec{K}_0 + \vec{G}. \qquad \text{(A11)}$$

For a nontrivial solution of (A9) to exist, the determinant of the matrix of coefficient must be zero, thus

$$(K - K_0)(K - K_G) = v_{\vec{G}} v_{-\vec{G}} / 4k_0^2. \qquad \text{(A12)}$$

In this equation we have made the approximations $K + K_0 \approx 2k_0$ and $K + K_G \approx 2k_0$. Equation (A12) defines the dispersion surface, that is, the locus of allowed internal incident wave vectors $\vec{K}_0$ in $\vec{k}$ space. The dispersion surface has two sheets, which are hyperbolas as shown in Fig. 24. We call the one branch of this surface α and the other branch β.

The neutron wave function must be continuous across the entrant surface. For perfect phase
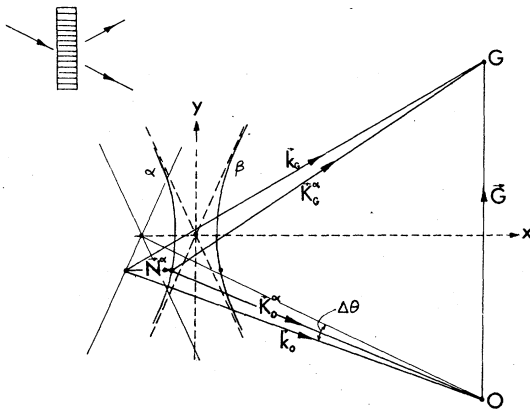
FIG. 24. Diagram showing the two hyperbolas of the dispersion surface giving the locus of the allowed internal wave vectors for the symmetric Laue case. The asymptotes (dashed lines) are circles of radii K [Eq. (A10)] drawn about the point O and the point G. The reciprocal lattice vector is $\vec{G}$ and $\vec{k}_0$ is the external incident wave vector.

matching, this requires that the internal wave vector $\vec{K}_0$ can differ from $\vec{k}_0$ by only a component normal to the surface. There are two possible values for $\vec{K}_0$ for each incident wave vector $\vec{k}_0$, one on the α branch and one on the β branch. Thus

$$\vec{K}_0^\alpha = \vec{k}_0 - \vec{N}^\alpha \qquad \text{(A13)}$$

and

$$\vec{K}_0^\beta = \vec{k}_0 - \vec{N}^\beta. \qquad \text{(A14)}$$

The relation between these vectors is shown in Fig. 24. Thus, the internal wave function is composed of four plane waves:

$$\psi(\vec{r}) = \psi_0^\alpha \exp(i\vec{K}_0^\alpha \cdot \vec{r}) + \psi_0^\beta \exp(i\vec{K}_0^\beta \cdot \vec{r})$$
$$+ \psi_{\vec{G}}^\alpha \exp(i\vec{K}_G^\alpha \cdot \vec{r}) + \psi_{\vec{G}}^\beta \exp(i\vec{K}_G^\beta \cdot \vec{r}). \qquad \text{(A15)}$$

The diffracted part of this wave function must be zero along the entrant boundary, and the incident part must match the external incident wave (A1). Thus,

$$\psi_{\vec{G}}^\alpha + \psi_{\vec{G}}^\beta = 0 \qquad \text{(A16)}$$

and

$$\psi_0^\alpha + \psi_0^\beta = \Phi. \qquad \text{(A17)}$$

The ratio of the diffracted wave amplitude $\psi_{\vec{G}}$ to the incident wave amplitude ψ_0 for each branch is determined by (A9). If we define C^γ to be $\psi_{\vec{G}}^\gamma / \psi_0^\gamma$ (where $\gamma = \alpha$ or β), then

$$C^\gamma = \frac{2k_0(K - K_0^\gamma)}{v_{-\vec{G}}} = \frac{v_{\vec{G}}}{2k_0(K - K_G^\gamma)}, \qquad \text{(A18)}$$

which are known for each incident wave vector $\vec{k}_0$. Thus, we can use (A16) and (A17) to express all of the internal wave amplitudes in terms of the amplitude of the incident wave Φ. The results are

$$\psi_0^\alpha = [C^\beta / (C^\beta - C^\alpha)]\Phi,$$
$$\psi_0^\beta = -[C^\alpha / (C^\beta - C^\alpha)]\Phi,$$
$$\psi_{\vec{G}}^\alpha = [C^\alpha C^\beta / (C^\beta - C^\alpha)]\Phi, \qquad \text{(A19)}$$
$$\psi_{\vec{G}}^\beta = -[C^\alpha C^\beta / (C^\beta - C^\alpha)]\Phi.$$

The wave function $\chi(\vec{r})$ emerging from the back face of the crystal is the sum of two coherent plane waves

$$\chi(\vec{r}) = \chi_0 \exp(i\vec{k}_0 \cdot \vec{r}) + \chi_G \exp(i\vec{k}_G \cdot \vec{r}). \qquad \text{(A20)}$$

The boundary condition for continuity of the neutron wave function across the back face of the crystal requires us to match the incident part of $\chi(\vec{r})$ with the incident part of $\psi(\vec{r})$, and also the diffracted part of $\chi(\vec{r})$ with the diffracted part of $\psi(\vec{r})$. The algebra is rather tedious, but straightforward. The results are

$$\chi_0 = \left(i \, \frac{\eta \sin\xi}{(\eta^2 + p^2)^{1/2}} + \cos\xi\right)e^{-i\delta_0}\Phi \qquad (A21)$$

and

$$\chi_{\vec{G}} = \left(i \, \frac{k_0}{v_{\vec{G}}} \, \frac{p^2}{(\eta^2 + p^2)^{1/2}} \sin\xi\right)e^{-i\delta_{\vec{G}}}\Phi , \qquad (A22)$$

where

$$\xi = a(\eta^2 + p^2)^{1/2}/2\cos\theta_B , \qquad (A23)$$

$$\delta_0 = a[(v_0/k_0) + \eta]/2\cos\theta_B , \qquad (A24)$$

$$\delta_{\vec{G}} = \delta_0 + 2k_0 a\Delta\theta \sin\theta_B . \qquad (A25)$$

The crystal thickness is a, θ_B is the nominal Bragg angle, and $\Delta\theta$ is the angular deviation of the incident wave vector $\vec{k}_0$ from the exact Bragg condition. The quantities p and η are given by

$$p = |v_G|/k_0 \qquad (A26)$$

and

$$\eta = k_0 \Delta\theta \sin2\theta_B . \qquad (A27)$$

The Fourier components of the neutron-crystal interaction potential are related to the structure factor F_G by

$$v_{\vec{G}} = 4\pi F_{\vec{G}}/V_{\text{cell}} , \qquad (A28)$$

where the volume of a unit cell is V_{cell}. The wave vector of the diffracted wave can be seen from the geometry of Fig. 24 to be

$$k_{\vec{G}} = \vec{G} + \vec{k}_0 + 2k_0\Delta\theta \sin\theta_B\hat{n} , \qquad (A29)$$

where $\hat{n}$ is a unit vector normal to the surface. Note that

$$|\chi_0|^2 + |\chi_G|^2 = |\Phi|^2 , \qquad (A30)$$

as it must, for the zero-absorption case we are considering.

[1]A. W. Overhauser and R. Colella, Phys. Rev. Lett. 33, 1237 (1974).
[2]R. Colella, A. W. Overhauser, and S. A. Werner, Phys. Rev. Lett. 34, 1472 (1975).
[3]S. A. Werner, R. Colella, A. W. Overhauser, and C. F. Eagen in Proceedings of the Conference on Neutron Scattering, Gatlinburg, Tennessee, 1976, pp. 1060–1072, ORNL Report No. ORNL-USERDA CONF 760601 (unpublished).
[4]S. A. Werner, J. L. Staudenmann, R. Colella, and A. W. Overhauser, in Proceedings of the International Workshop on Neutron Interferometry, Grenoble, France, edited by U. Bonse and H. Rauch (Oxford University Press, New York, to be published).
[5]S. A. Werner, J. L. Staudenmann, and R. Colella, Phys. Rev. Lett. 42, 1103 (1979).
[6]U. Bonse and M. Hart, Appl. Phys. Lett. 6, 155 (1965).
[7]H. Rauch, W. Treimer, and U. Bonse, Phys. Lett. 47A, 425 (1974).
[8]For recent reviews of neutron and x-ray interferometry see U. Bonse and W. Graeff in X-ray Optics, Topics in Applied Physics, edited by H-J. Queisser (Springer, Berlin, 1977), Vol. 22; H. Rauch and D. Petroschek, in Neutron Diffraction, edited by H. Dachs (Springer, Berlin, 1978), pp. 303–351.
[9]J. W. T. Dobbs, J. A. Harvey, D. Daya, and H. Horstmann, Phys. Rev. 139, 756 (1965).
[10]L. Koester, in Neutron Physics (Springer, Berlin, 1977), pp. 1–15.
[11]R. Eötvös, Math. Nat. Ber. Ungarn. 8, 65 (1890); R. Eötvös, D. Pekárand and E. Fekete, Ann. Phys. (N.Y.) 68, 11 (1922); P. G. Roll, R. Krotkov, and R. H.

Dicke, Ann. Phys. (N.Y.) 26, 442 (1967).
[12]For a discussion of this point see D. M. Greenberger and A. W. Overhauser, Rev. Mod. Phys. 51, 43 (1979).
[13]A. A. Michelson, H. G. Gale, and F. Pearson, Astrophys. J. 61, 140 (1925).
[14]M. G. Sagnac, C. R. Acad. Sci. (Paris) 157, 708 (1913); 157, 1410 (1913).
[15]An early attempt to achieve neutron interferometry was made by H. Maier-Leibnitz and T. Springer, Z. Phys. 167, 386 (1962), using a prism as a beam splitter.
[16]W. Bauspiess, U. Bonse, and W. Graeff, J. Appl. Crystallogr. 9, 68 (1976).
[17]W. Bonse and E. teKaat, Z. Phys. 243, 14 (1971).
[18]L. D. Landau and E. M. Lifshitz, Mechanics, 2nd ed. (Pergamon, New York, 1969), pp. 126–129.
[19]L. A. Page, Phys. Rev. Lett. 35, 543 (1975).
[20]J. Anandan, Phys. Rev. D 15, 1448 (1977).
[21]L. Stodolsky, in Proceedings of the International Conference on Neutron Interferometry, Grenoble, France, edited by U. Bonse and H. Rauch (Oxford Univ. Press, New York, to be published).
[22]M. Dresden and C. N. Yang, Phys. Rev. D 20, 1846 (1979).
[23]S. A. Werner, Phys. Rev. B 21, 1774 (1980).
[24]B. W. Batterman and H. Cole, Rev. Mod. Phys. 36, 681 (1964).
[25]H. A. Rauch and D. Petroschek, in Neutron Diffraction, edited by H. Dachs (Springer, Berlin, 1978), pp. 303–351.
[26]U. Bonse and W. Graeff, in X-ray Optics, Topics in Applied Physics, edited by H.-J. Queisser (Springer, Berlin, 1977), Vol. 22, pp. 93–143.